# Simultaneous ELM Suppression and Divertor Detachment via Synergistic Boron Powder and Neon Injection in EAST

Zhen Sun[1]*, Rajesh Maingi[1], Wei Xu[2], Lei Peng[3], Kedong Li[2]*, Xin Lin[2], Yunxin Cheng[2], Donggui Wu[2], Fang Ding[2], Zhe Wang[2], Yanhong Guan[2], Minrui Wang[2], Yan Chao[2], Qingquan Yang[2], Kaifu Gan[4], Yuqiang Tao[5], Alessandro Bortolon[1], Huiqian Wang[6], Tianfu Zhou[2], Jia Huang[2], Wei Wang[2], Yifei Jin[2], Yanmin Duan[2], Yanzhen Xu[2], Ahmed Diallo[1], Kevin Tritz[7], Alexander Nagy[1], Hanna Schamis[1], Guizhong Zuo[2]*, Jinping Qian[2], Xianzu Gong[2], Jiansheng Hu[2], and EAST Team

[1]Princeton Plasma Physics Laboratory, Princeton, NJ 08540, USA

[2]Institute of Plasma Physics, Chinese Academy of Sciences, Hefei, Anhui 230031, China

[3]Henan University of Engineering, Zhengzhou, Henan 451191, China

[4]University of Tennessee, Knoxville, Tennessee 37996, USA

[5]Anhui Normal University, Wuhu, Anhui 241000, China

[6]General Atomics, San Diego, CA 92186, USA

[7]Johns Hopkins University, Baltimore, MD 21211, USA

*corresponding authors: kdli@ipp.ac.cn, zuoguizh@ipp.ac.cn, zsun@pppl.gov

## Abstract

A novel approach for simultaneous power exhaust and edge-localized mode (ELM) control is presented in the Experimental Advanced Superconducting Tokamak discharges, which utilize an ITER-like tungsten divertor. Real-time injection of boron (B) powder and neon (Ne) gas overcomes their limitations encountered when used separately. Pure Ne seeding leads to a narrow operational window constrained by core impurity accumulation and H-mode to L-mode back transitions, while pure solid B powder injection (SBI) is insufficient for effective divertor cooling. In comparison, their combined use achieves a stable, stationary, ELM-suppressed H-mode with adequate power exhaust. This synergistic scenario features partial energy detachment at the outer divertor while maintaining good plasma confinement ($H_{98}$ ~ 1) with minimal degradation. Two key features of this scenario are: 1) the SBI triggers a persistent Edge Harmonic Mode (EHM), which provides a crucial continuous particle transport channel, preventing Ne and tungsten/ molybdenum accumulation without flushing out by ELM, and 2) the B+Ne mixture allows for active optimization of the radiated power profile. Core radiation can be reduced by substituting a portion of the Ne with B, leveraging their complementary non-coronal equilibrium radiation efficiencies. This combined B+Ne injection scheme presents a promising pathway toward integrated core-edge scenarios, offering the potential to minimize total impurity throughput while leveraging an actuator (powder injection) already being considered for ITER.

## Key words

Boron, Neon, ELM, detachment, core edge integration

# 1. Introduction

The successful operation of next-generation tokamak experiments, such as ITER, is critically dependent on the development of robust plasma scenarios that can simultaneously handle two major core-edge integration challenges: mitigating the intense, steady-state heat to the divertor targets, and suppressing or mitigating large, transient heat loads from Type-I edge-localized modes (ELMs) [1-3].

Divertor power exhaust management typically relies on inducing a state of partial or full thermal plasma detachment through impurity line radiation. Neon (Ne) and Argon (Ar), in particular, are attractive radiators for ITER due to their high radiation efficiency and chemical inertness [4-6]. Indeed, Ne seeding has demonstrated the capability to robustly reduce inter-ELM divertor heat flux via partial detachment across multiple major tokamaks. When operated within the right window of heating power, density, and Ne dose, this can be achieved while maintaining, or in some cases even improving, core plasma performance [7-9]. Recent integrated scenarios have shown good progress: JET has demonstrated scenarios with Ne that simultaneously enable high divertor radiation, the absence of large ELMs, and acceptable normalized performance (e.g., normalized confinement factor $H_{98} \approx 0.9$, normalized beta $\beta_N \approx 2.2$ at high power with Ne concentration $C_{Ne} \approx 1–2\%$) [8,10,11]. Similarly, EAST has achieved sustained ELM suppression and stable partial detachment, with the strike point temperature falling from >40 eV to <5 eV and the stationary heat flux reduced by >90% in the ELM-free phase, all while maintaining $H_{98}>1$ [9]. In DIII-D high-$\beta_p$ plasmas, careful Ne optimization has led to deep detachment together with complete ELM suppression, where the H-mode pedestal degradation was offset by a strong internal transport barrier (ITB), preserving high global performance ($\beta_N \approx 2.8$) [7].

However, despite these successes, these multi-machine experiments have consistently revealed fundamental limitations that create a narrow and precarious operational window. A primary challenge occurs when heating power is too low, or the Ne rate is too high, leading to excessive drops in the H-mode pedestal temperature. This can lower the power crossing the separatrix ($P_{SOL}$) relative to the L-H transition power threshold, triggering M-mode dithering [12] or net H→L transitions, a phenomenon observed at JET at moderate heating power with high Ne radiative fractions [13]. A more pervasive issue is excessive core radiation and fuel dilution. In DIII-D high-$\beta_p$ plasmas, for example, Ne injection often leads to non-stationary density evolution and high $Z_{eff}$ (up to ~5), requiring further development of impurity or density control techniques [14]. As observed in ASDEX-Upgrade, altering the pedestal with impurity seeding to suppress ELMs can, in turn, reduce the impurity flushing mechanism provided by ELMs, leading to a tendency toward impurity accumulation and potential disruption [15]. Finally, operational constraints, such as re-ionization heat loads on limiters in JET D–T experiments, can further narrow the already tight window for successful Ne integration [8].

Boron (B), injected as a powder, has shown excellent real-time wall conditioning effects on multiple devices [16-21]. Recognizing these benefits and with its plan to operate with a full tungsten wall, ITER is now considering solid B injection (SBI) as a primary tool for oxygen gettering [22,23]. Furthermore, B has been shown to be an effective tool for ELM suppression [24-28]. B also has favorable radiative properties at relatively low electron temperature ($T_e$), typical of approaching detached divertor conditions [19,29,30]. However, its own capability as a radiator is insufficient for significant outer divertor cooling in the hotter scrape-off layer (SOL) [6,29]. While real-time boron powder injection offers significant advantages for ELM suppression and wall conditioning, its application in steady-state fusion reactors requires careful consideration of the material lifecycle. Unlike gaseous impurities that are pumped out, solid boron eventually migrates from plasma-wetted surfaces to magnetically shadowed regions, such as the inner divertor baffles [3,31]. In a D-T reactor environment, these accumulated boron layers can co-deposit with tritium, potentially impacting the in-vessel fuel inventory. Consequently, the implementation of this technique in future devices must be coupled with established fuel recovery strategies—such as Ion Cyclotron Wall Conditioning (ICWC), localized surface heating (e.g., strike-point sweeping), or physical slag removal [32]—to mitigate tritium retention in the shadowed regions [33].

This paper presents a novel approach that overcomes these limitations by synergistically injecting solid B and Ne gas. The proposed scheme aims to leverage the strengths of both species while mitigating their weaknesses, operating through two interconnected mechanisms. We will show that a B-induced Edge Harmonic Mode (EHM) provides a critical, continuous impurity exhaust channel, fundamentally addressing the core contamination and stability issues that plague pure-Ne scenarios. Following the experimental setup, the results demonstrating this dual mechanism will be presented, followed by a discussion of the implications in the context of international research, and a summary and outlook.

## 2. Experimental Setup

The experiments were conducted on the EAST device with a tungsten divertor [34] in an upper-single-null (USN) magnetic configuration, with the ion B×∇B drift directed toward the active X-point ("favorable" configuration). The plasma parameters were maintained with plasma current $I_p$ ~ 0.5 MA, toroidal magnetic field $B_{t0}$ ~ 2.4 T, safety factor $q_{95}$ ~ 5.3, lower triangularity $\delta_L$ ~ 0.6, and upper triangularity $\delta_U$ ~ 0.32. The plasmas were heated with ~ 3.5 MW of combined lower hybrid wave (LHW ~ 2.6 MW) and electron cyclotron resonance heating (ECH ~ 0.9 MW) at the axis, sustaining them in the H-mode from t ~ 2.6 s. The $I_p$ flattop phase is from 2.4s to 7.5s, and the strike point is fixed during the flattop phase.

Two independent impurity injection systems were employed (Figure 1). SBI of crystalline B powder (>99.9% purity, ~70 µm grain size) was performed using an Impurity Powder Dropper (IPD) [35] located at a top port, at rates of ~1-12×$10^{20}$ B atoms/s. Ne gas (50% Ne, 50% $D_2$) was injected through a piezoelectric valve at the upper outer (UO) divertor target, with total particle injection rates of 1.0-1.4×$10^{20}$ atom $s^{-1}$. The distance of the Ne inlet to the divertor corner (X) is 11.35cm. The IPD powder drop rate is calibrated offline versus the applied control voltage and cross-validated using an optical flowmeter and the injector vibration amplitude measured by an accelerometer. During operation, the powder flow is monitored in real time by the flowmeter (≈5% accuracy) and checked using the accelerometer signal; the resulting SBI rate is typically controlled within ≈5–10%. The neon piezo-valve injection rate is calibrated offline versus the command voltage and monitored/calibrated using the gas-tank pressure-drop method (PV = nRT), yielding ≈1–2% calibration accuracy. IPD-based wall-conditioning feedback and neon-based divertor-detachment feedback control have been successfully applied on EAST [36,37].

A series of discharges was conducted to systematically investigate these effects. The key parameters and injection schemes for the discharges discussed in this paper are summarized in Table 1, which serves as a reference for the following sections.

Table 1 *Summary of key experimental discharges. (Table header describes the columns: discharge number, B flow rate, SBI start time to end time, Ne injection rate, Ne injection duration, key control actions, and observed plasma response.)*

| Discharge | B rate (1E20 atom/s) | SBI time (s) | Ne rate (1E20 atom/s) | Ne time (s) | Key control action | Plasma response |
|---|---|---|---|---|---|---|
| 93185 | - | - | 1.1 | 4.5-6.32 | OSP shifted near Ne inlet, X = 9.5 cm to Div. corner | ELM suppression<br>Te@OSP ~ 16eV<br>H-L @ 7.4 s |
| 93186 | - | - | 1.1 | 4.5-6.32 | OSP shifted to Div. corner, X= 6.5 cm | ELM mitigation<br>Te@OSP ~ 21 eV<br>$H_{98}$ 1.2 → 1.1 |
| 93187 | - | - | 1.15 | 4.5-5.97 | Increased first two pulses, short duration | ELM mitigation<br>Te@OSP ~ 25 eV<br>W ramp-up |
| 93188 | - | - | 1.2 | 4.5-6.32 | Increased Ne rate | ELM suppression<br>Te@OSP ~ 9 eV<br>H-L @ 6.5 s |
| 93191 | 5 | 3-6.5 | 1.2 | 5-6.85 | Added B to Ne rate of #93188 | ELM suppression<br>Te@OSP ~ 16 eV<br>$H_{98}$ 1.2 → 1.06 |
| 93192 | 3.9 | 3-6.5 | 1.4 | 5-6.9 | Decreased B, increased Ne | ELM suppression<br>Te@OSP ~ 5.5 eV<br>$H_{98}$ 1.3 → 0.95 |
| 93193 | 5 | 2-8.5 | 1.3 | 5-6.87 | Extended B duration, decreased Ne | ELM sup. from L-H<br>Te@OSP ~ 8 eV<br>$H_{98}$ 1.05 → 0.95 |
| 93194 | 5 | 4-8.5 | 1.3 | 3.5-6.38 | Time sequence reversal: Ne first, B later | Avoided H-L<br>Te@OSP ~ 5.5 eV<br>$H_{98}$ 1.22 → 0.92 |

A suite of diagnostics was employed to monitor the plasma response to impurity injection [24], as illustrated in Figure 1. The poloidal layout shows key measurements relative to the plasma equilibrium. A 64-channel absolute extreme ultraviolet (AXUV) photodiode array measures the plasma radiation profiles [38]. Two flat-field grazing incidence extreme ultraviolet (EUV) spectrometers monitor the intensity of highly-ionized impurity emission, including B-V (λ = 4.098 nm), Ne-IX (1.355nm), and W-UTA (unresolved transition array) for tungsten [39]. Divertor conditions are monitored by triple Langmuir probe (LP) arrays on the inner and outer target plates, providing ion saturation current and $T_e$ [40]. A filter-scope system measures Dα emission, and a multichannel visible spectroscopy diagnostic views the outer target to monitor neutrals and low-

Z impurities. Two poloidal visible bremsstrahlung sighting lines are used to calculate the line-averaged effective ion charge, $Z_{eff}$, with input of $T_e$ and $n_e$ at the tangential magnetic surface [41]. The uncertainty of the $Z_{eff}$ calculation is ~ 30%. Two neutral pressure gauges (Pfeiffer PRK251) are located at the top and midplane of the vessel.

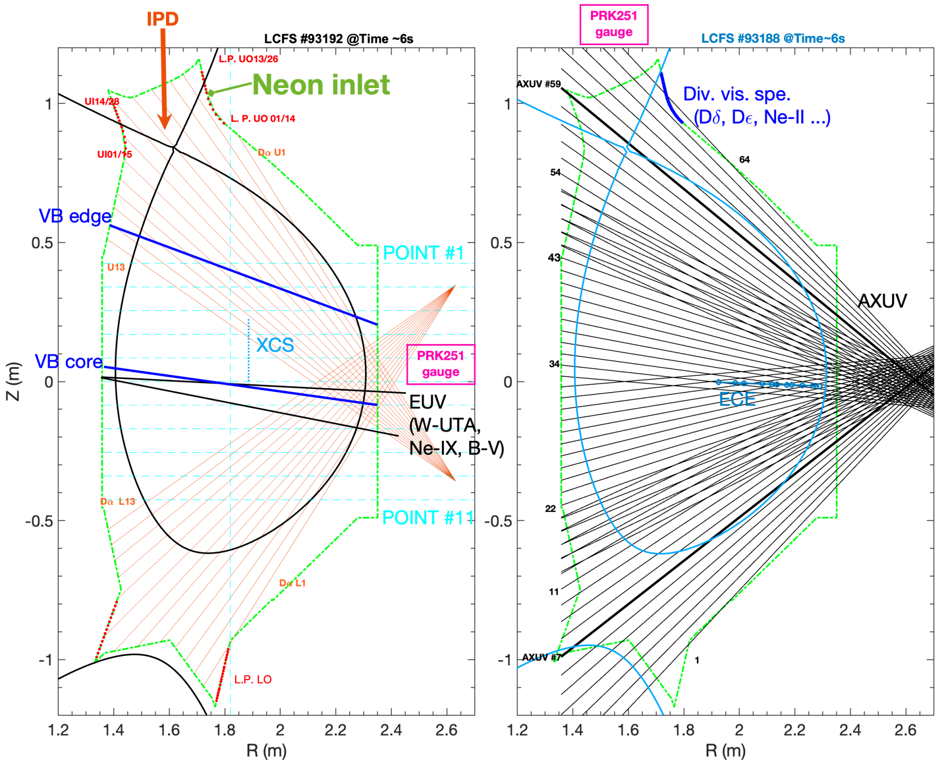


Figure 1 ***Poloidal layouts of primary diagnostics for upper-single-null discharges**. The reconstructed equilibria for discharge #93192 and #93186 at t = 6 s are shown. (Left panel) Locations of the Ne gas inlet, divertor Langmuir probes (LP), upper & lower Da arrays, EUV spectrometer sightline, 11-channel polarimeter-interferometer (POINT), x-ray imaging crystal spectrometer(XCS), and two neutral pressure gauges. (Right panel) Sightlines for the 64-channel AXUV bolometer array, multi-channel middle-plane electron cyclotron emission (ECE), and divertor visible spectroscopy. The orange arrow indicates the downward trajectory of injected B powder from the IPD.*

The fundamental physics motivating the mixed-radiator approach is illustrated by the impurity cooling factor curves shown in Figure 2. In the high-density, low-temperature plasma typical of a divertor, impurities do not reach coronal equilibrium (CE) due to their short residence times (τ). This non-coronal equilibrium (NCE) state significantly alters their radiative properties. The parameter $n_e\tau$ (electron density × residence time) characterizes the deviation from CE (solid lines). For the NCE conditions expected in the plasma edge (lower $n_e\tau$ values), B's radiation efficiency ($L_z$) is strongly enhanced compared to its CE value. For instance, considering a proxy transit time τ of 0.2ms (estimated from the connection length and ion sound speed in the SOL), the NCE radiation curve (solid red line) shows that B's $L_z$ is not only enhanced but also extends its effective radiating range to higher temperatures, up to ~20 eV, where it can exceed that of Ne, under the right conditions. Scenarios with particle recycling or oscillation could lead to even shorter residence times. Conditions with even shorter residence times (e.g., τ = 0.01ms, dashed lines) show that B's radiation capability can be stronger than Ne's up to $T_e$ ~ 500 eV. ASDEX-Upgrade reports that the deposited B is the contributor to the missed power loss via the SOLPS simulation [30]. This atomic physics behavior is key: under realistic edge conditions, B becomes a much more potent radiator than CE predictions suggest. This provides a rationale with concurrent B and Ne injection, as the enhanced radiation from B can take on a significant portion of the cooling burden.

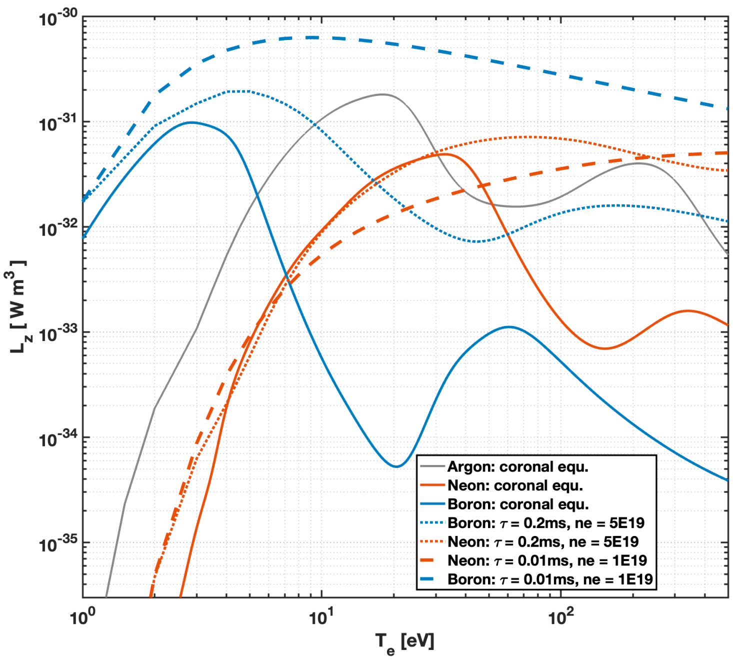


Figure 2 ***ADAS-calculated [42] cooling factors $L_z$ ($T_e$) for B and Ne.*** *The curves show the radiation efficiency under coronal equilibrium (CE, solid lines) and non-coronal equilibrium (NCE, dot and dashed lines) conditions for different values of the parameter $n_e\tau$. Under NCE, B's radiation is significantly enhanced and extended to higher temperatures.*

# 3. Experimental Results

## 3.1. Independent Injection of B and Ne: Operational Limits

First, to establish a baseline for the synergistic experiments and to demonstrate their individual limitations, the effects of injecting B powder and Ne gas independently were characterized. The results show that while SBI can effectively suppress ELMs and the plasma exhibits a high tolerance to it, its capability for achieving divertor radiative cooling is limited.

Figure 3 illustrates the plasma response to SBI alone. The left-hand side panels compare three discharges: no B (#93154), low-rate SBI (#93159, ~2.5mg/s-1.4×$10^{20}$ atom/s), and high-rate SBI (#93179, ~15mg/s-8.4×$10^{20}$ atom/s). **Panel (a)**, showing the B-V emission, and **panel (b)**, showing the Dα signal, clearly indicate that ELMs are fully suppressed with a sufficient SBI rate. A key finding is that a low SBI rate (#93159) was sufficient to maintain ELM suppression while preserving a high confinement factor ($H_{98}$) nearly identical to the no-B case, as seen in **panel (c)**. When the SBI rate was increased 6 times relative to #93159 (in discharge #93179), the plasma remained in H-mode, albeit with a noticeable decrease in $H_{98}$ and an increase in $n_e$. This demonstrates a wide operational window of B rate and high plasma tolerance for B powder. The wide range is beneficial for control. The continuous SBI also improved wall conditions, as evidenced by the decrease in the O-VIII impurity proxy in **panel (e)**, a behavior similar to that observed for tungsten and molybdenum impurities.

The right-hand side panels reveal further details of the SBI effects. **Panel (f)** shows the cross-power spectrogram of AXUV and Dα signals for the low-rate case (#93159), which clearly indicates the presence of an EHM [24,25,27,43]. Multiple edge low-frequency fluctuations are known to occur in inner or both targets detached divertor conditions[43]; here, we use 'EHM' as an operational label for the SBI-correlated low-frequency band relevant to impurity control in this dataset, but disentangling and classifying these modes is beyond the scope of this work. The key trends reported here are unchanged when the EHM metric is evaluated over a broader low-frequency band. **Panel (g)** plots the ratio of two AXUV chord signals for all three discharges: a chord viewing the plasma edge near the upstream separatrix (AXUV #7, see Figure 1) and another viewing slightly deeper into the core (AXUV #10). Each AXUV channel measures a line integral of emissivity over its line-of-sight (LOS) and spectral response, which can be expressed as

$$S_i(t) = \int_\lambda R_{AXUV}(\lambda) \int_{LOSi} \varepsilon(r,\lambda,t)\, d\lambda\, dl \approx \int LOS_i\ w_i(r)\, P_{rad}(r,t)\, dl,$$

where $w_i$ absorbs optics and response factors, and $P_{rad}(r) = n_e^2 C_{brem}(T_e) + \sum_z n_e n_Z L_Z(T_e)$ is the local radiated power density. Using fixed-view AXUV chords on EAST, the ratio increased during SBI while B-V visible emission rose, indicating a preferential increase of chord-integrated emissivity in the near-separatrix/SOL region emphasized by chord #7; the lack of further rise in between low and high injection rates is consistent with saturation of edge-localized radiative losses approaching the geometric weighting limit of the chords; given the cooling factor of B peaks at a few–10 eV, these observations are consistent with SOL-localized radiation rather than core radiation. This strongly suggests that B's radiative contribution is predominantly localized at the edge region, near the separatrix, or in the SOL. This could imply that B ions are also potentially confined to the edge region, but it does not support the view that they are mainly located there and avoid significant core fuel dilution. Unfortunately, the B concentration is not available to confirm core dilution. ASDEX-upgrade shows that B-ion density profiles vary from very hollow to flat or peak at mid-radius in H-mode discharges with SBI or modulated heating using the B-coated antennas [20,44]. With EAST plasma parameters, SOLPS-ITER simulations show $Z_{eff}$ increases from ~3% at 2cm inside the midplane separatrix to ~25% at the midplane separatrix [45,46]. Despite these positive effects, B's capability for power exhaust is limited. The panels for the high-rate discharge #93179 (**panels h, i, and j**) show that while SBI drove the inner divertor target into particle detachment (significant ion saturated current ($J_{sat}$) reduction in **panel h**), the outer target remained attached (**panel i**). The outer target temperature (**panel j**) was only modestly reduced from ~65 eV to ~45 eV, far from the conditions required for energy detachment.

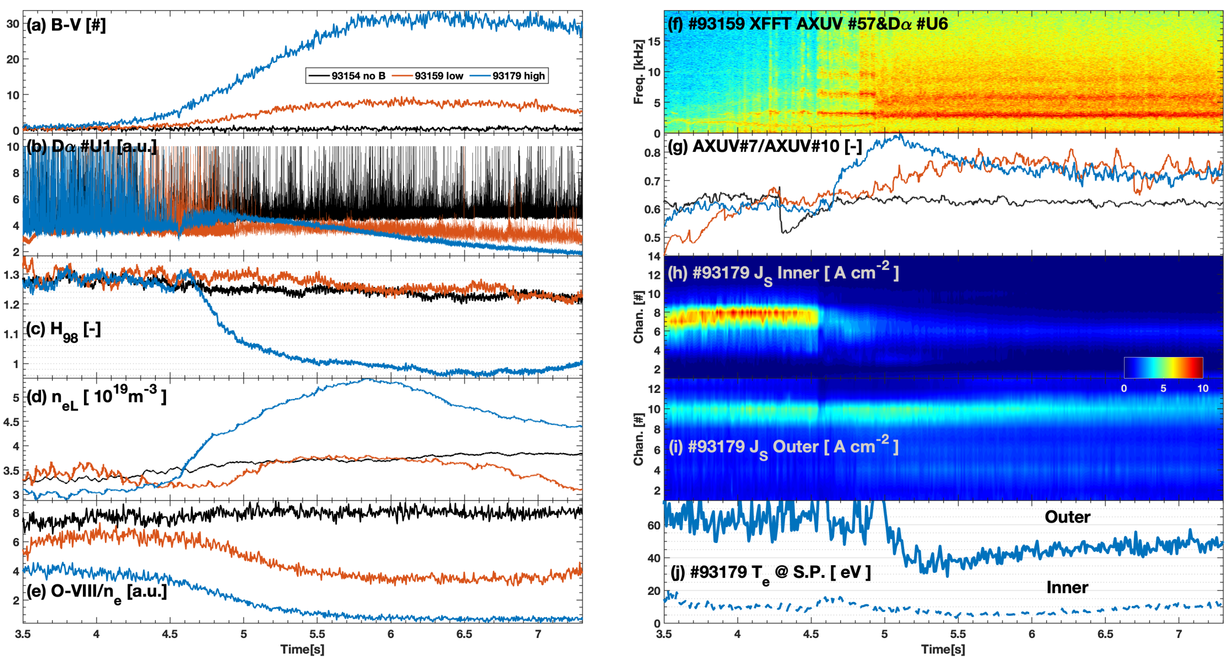


Figure 3 ***ELM suppression by SBI alone and its limited effect on outer target cooling.*** *Left panels compare discharges with no B (#93154), low-rate SBI (#93159), and high-rate SBI (#93179); (a) B-V emission; (b) Dα emission; (c) $H_{98}$ confinement factor; (d) Line-averaged density; (e) O-VIII impurity proxy. Right panels show further details: (f) cross-power spectrogram of AXUV #57 and Dα #U6 for #93159, showing the EHM; (g) Ratio of AXUV channels #7 (around tangential separatrix) and #10 (through pedestal) for all three discharges, indicating edge-localized radiation; (h, i) $J_{sat}$ on the inner and outer targets for #93179, showing inner-target particle detachment; (j) $T_e$ at the strike points for #93179.*

Experiments with Ne injection alone for power exhaust control identified a narrow and difficult-to-control operational window, as the plasma is highly sensitive to the injection rate. In a representative case (#93186, Figure 4), a small Ne injection rate of $1.1 \times 10^{20}$ atom/s led to ELM mitigation but not full suppression. While the outer strike point $T_e$ was reduced, it was not low enough to achieve energy detachment. It was also observed (though not shown in a figure) that the tungsten concentration gradually increased with Ne injection.

When the injection rate was increased by only 9% to $1.2 \times 10^{20}$ atom/s in discharge #93188, the plasma response changed dramatically. This slightly higher rate was sufficient to trigger outer target detachment but was unsustainable. The discharge experienced significant particle accumulation, a continuous drop in stored energy, and ultimately underwent an H-L back-transition at t~6.5s. Another discharge (#93185), despite having a lower injection rate than #93186, resulted in a similar H-L transition (see Table 1), due to the strike point being closer to the gas inlet valve, leading to more ionization **[47]**. Together, discharges #93188 and #93185 provide strong evidence that pure Ne injection is prone to performance degradation and plasma collapse due to either global accumulation or local "self-poisoning." These representative results highlight the significant challenge of using Ne alone for simultaneous ELM control and divertor detachment.

## 3.2. Synergistic ELM Suppression and Divertor Detachment with Simultaneous B and Ne

The central result of this work is that the combined, synergistic injection of B and Ne overcomes their individual limitations. Figure 4 directly compares discharges to illustrate this synergy. The left side (#93191 vs #93186) shows that at a lower Ne rate, adding B achieved complete ELM suppression and a lower divertor temperature, a state inaccessible to the Ne-only case. The right side (#93192 vs #93188) shows that at a higher Ne rate, adding B prevented the H-L back-transition and uncontrolled density rise seen in the Ne-only case, achieving a stable, stationary operating point. It is noteworthy that while #93191 and #93188 have the same total Ne injection rate, their outcomes are drastically different, underscoring the stabilizing role of B.

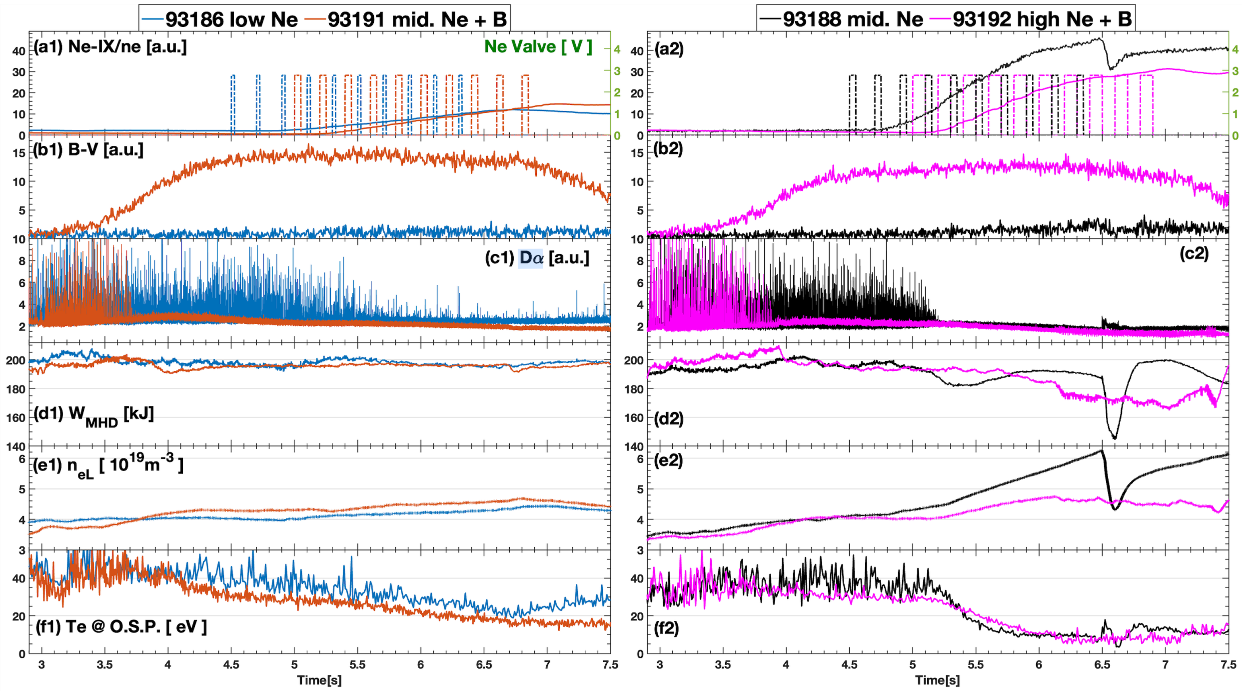


Figure 4 ***Comparison of discharges preliminary demonstrating the expanded operational window with SBI+Ne.*** *Left side: #93191 orange vs #93186 blue; right side: #93192 magenta vs #93188 black; (a) left-Y: midplane Ne-IX/$n_e$, right-Y: control voltage wave for the piezoelectric valve; (b) B-V emission intensity; (c) Dα emission; (d) plasma stored energy given by EFIT; (e) line-averaged density; (f) electron temperature measured by LP near the outer strike point.*

This synergistic scheme not only stabilizes the plasma edge but also maintains core performance well, in stark contrast to the degradation observed with pure Ne injection. Figure 5 presents a comparison of plasma profiles at several time slices for the unstable pure Ne discharge (#93188) and the stable synergistic discharge (#93192). Unfortunately, Thomson Scattering data were unavailable, so the density profiles were constructed by combining data from the POINT (POlarimeter-INTerferometer) system, an 11-channel diagnostic measuring line-integrated density, and an edge reflectometer. $T_e$ profiles are from ECE (Electron Cyclotron Emission), but the data in the pedestal region are unreliable due to insufficient optical thickness and are therefore not shown. The $T_i$ data is limited to the core from XCS (X-ray Crystal Spectrometer) measurements, which have relatively large error bars. Despite these limitations, the profile comparison reveals key physical differences. **Panel (a)** shows that during the cooling phase of the pure Ne discharge (#93188 at 6.4s), the density profile tends to rise across the board. In contrast, the density is more controllable in the stable, detached phase of the B+Ne case (#93192 at 6.7s). Both B and Ne injection lead to a decrease in core $T_e$ (**panel b**), which is an expected consequence of the density rise. However, a remarkable result is seen in the core $T_i$ (**panel c**): in the stable B+Ne phase, $T_i$ not only avoids degradation but actually increases. This ability to maintain or even improve core $T_i$ is a significant advantage of the synergistic approach. Since the auxiliary heating is predominantly RF electron heating and $T_i < T_e$ in these discharges, the increase of core $T_i$ is consistent with enhanced electron-ion collisional energy transfer as the density and collisionality rise during the seeded stationary phase ($P_{ei} \propto n_e^2(T_e - T_i)T_e^{-3/2}$). While impurity seeding may also contribute to ion heat transport reduction through turbulence stabilization, as discussed in prior modeling [48,49], the decrease in core $T_e$ is not the typical signature of turbulence suppression. Quantifying the relative contributions of equipartition versus transport requires dedicated power-balance analysis, which is left for future work.

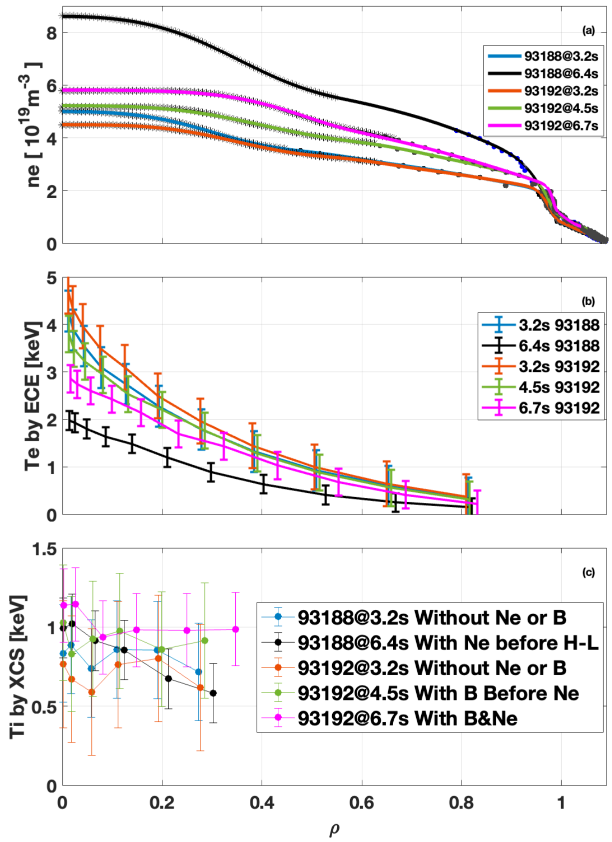


Figure 5 ***Plasma profiles for Ne alone (#93188) and synergistic B+Ne (#93192) discharges.*** *Time slices are shown for before SBI or Ne seeding (3.2s), during SBI before Ne injection (#93192 at 4.5s), during Ne seeding before collapse (#93188 at 6.4s), and during stationary synergistic operation (#93192 at 6.7s). (a) $n_e$ profiles from POINT and reflectometry. (b) $T_e$ profiles from ECE. (c) $T_i$ profiles from XCS.*

Successful core and edge integration occurred via B+Ne injection. Figure 6 provides a detailed, multi-diagnostic showcase of the successful synergistic discharge #93192, confirming a state of partial energy detachment without particle detachment [50,51]. **Panel (a)** shows the steady impurity injection. The Langmuir probes in **panel (b)** indicate a drop near the outer strike point $T_e$ to below 10 eV, while the far SOL remains hotter, signifying localized cooling. This is independently supported by the spectroscopic measurement in **panel (c)**, which shows the intensity ratio of two deuterium Balmer lines (Dε, n=7→2 at 396.90 nm to Dδ, n=6→2, at 410.06 nm). This ratio is sensitive to $T_e$ in the recombination-dominated regime below ~5 eV; a sharp increase in the Dε/Dδ ratio is a signature of a cooling, recombining plasma [52]. This energy dissipation provides effective target protection, as shown by the IR thermography in **panel (d)**, where the peak surface temperature drops from ~300°C to ~100°C. However, the $J_{sat}$ profile in **panel (e)** shows that the particle flux increases after Ne injection and remains attached, confirming this as a state of energy detachment, not particle detachment. Furthermore, **panel (f)** shows a significant increase in the ratio of divertor to mid-plane neutral pressure (the compression ratio), which is an accompanying feature of detachment, indicating enhanced recycling and neutral density in the divertor.

Throughout this detached phase, core performance is well maintained. Core $T_e$ decreases but core $T_i$ increases (**panels g, h**), consistent with the profile data in Figure 5. **Panels (i)** and **(j)** provide crucial information on fuel ion dilution. $Z_{eff}$, calculated from line-integrated visible bremsstrahlung, increases with B and Ne injection. **Panel (i)** shows two $Z_{eff}$ measurements: one from a central chord (VB core) and one from a chord viewing the plasma edge (VB edge, see Figure 1). A central $Z_{eff}$ increased from ~1.4 to ~2.5 directly implies that impurity ions are displacing the primary fuel ions (deuterium). Notably, the edge $Z_{eff}$ rises more significantly, suggesting a higher concentration of impurities in the plasma edge region compared to the deep core. However, despite this increase in $Z_{eff}$, the neutron rate measured by both the $^3$He detector and the $^{235}$U fission chamber, a proxy for fusion performance, not only avoids a decrease but actually increases (**panel j**).

A careful interpretation is required. A simple estimation can be made: assuming the $Z_{eff}$ from the central chord increases from 1.4 to 2.0, it is solely due to B. Assuming the $Z_{eff}$ rise is entirely due to fully stripped B, the Deuterium fraction, $n_D/n_e = 1 - Z_B(n_B/n_e)$ with $n_B/n_e = (Z_{eff} - 1)/(Z_B^2 - Z_B) = 2\%$, drops from ≈ 90% at $Z_{eff}$ ≈ 1.4 to $n_D$/ne ≈ 75% at $Z_{eff}$ ≈ 2.0, corresponding to about 17% relative fuel dilution and a B fraction $n_B$/ne increasing from ≈2% to ≈ 5%. Assuming the further increase to 2.5 is solely due to Ne, the added Ne fraction is $n_{Ne}/n_e = (2.5 - 2)/(Z_{Ne}^2 - Z_{Ne}) = 0.56\%$, and the fuel-ion fraction ($n_D/n_e = 1 - Z_{Ne}(n_{Ne}/n_e)$) drops from 75% to 69.4%, i.e., an extra 5.6% absolute (7.4% relative) dilution on top of the B case. Note that the $Z_{eff}$ is a chord-weighted quantity, so these results represent LOS-averaged dilution. This yields bounds: if the entire rise from 1.4 to 2.0 is edge-only, core dilution is minimal; if the rise is uniform, $n_{D\_core}/n_e \approx 70\%$, implying ~20% relative core dilution. The higher values measured by the edge-viewing chord suggest that dilution is likely more pronounced at the edge than in the core. The neutron rate is proportional to the square of the deuterium density and the fusion reactivity, which is a function of $T_i$. In this case, the increases in both $n_e$ and $T_i$ are expected to significantly boost the neutron rate, likely overwhelming any negative effect from fuel dilution. Therefore, although neutron data alone cannot confirm the absence of core fuel dilution, the combination of a smaller increase in core $Z_{eff}$, rising $T_i$, and a steady neutron rate strongly suggests that the synergistic injection scheme did not cause significant core fuel ion dilution and effectively contained the negative effects of impurities.

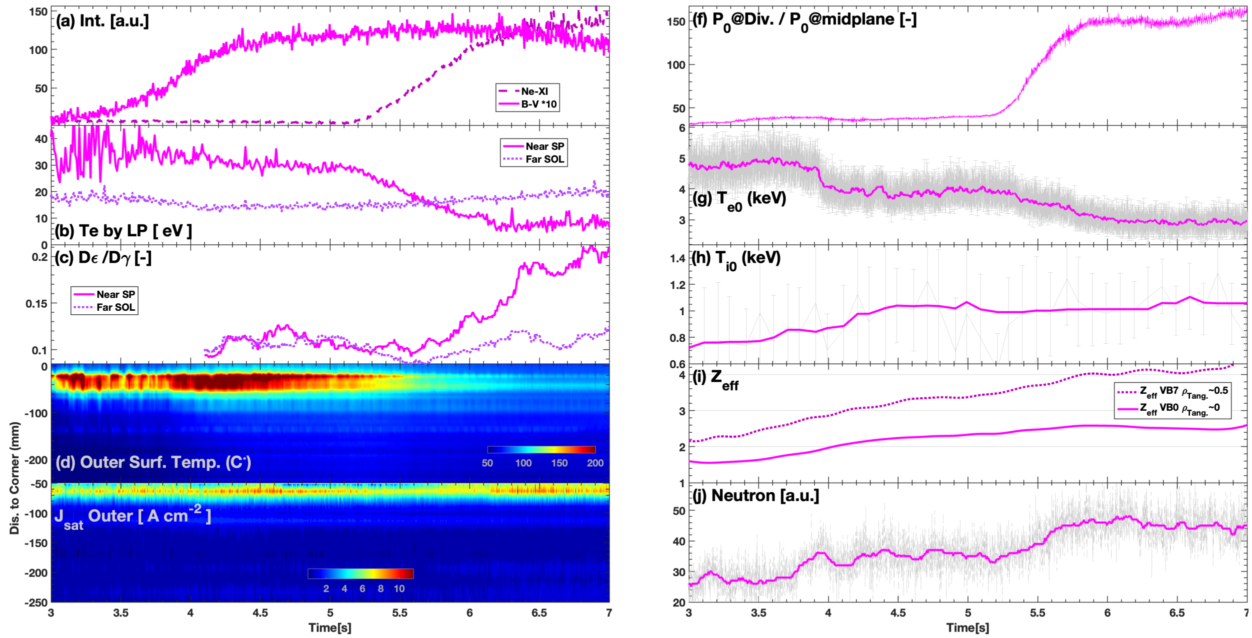


Figure 6 ***Detailed characterization of a successful synergistic B+Ne discharge (#93192).*** *(a) B-V and Ne-IV emission. (b) Outer target Te. (c) Dε/Dδ line intensity ratio. (d, e) 2D profiles of IR surface temperature and Jsat. (f) Ratio of divertor to mid-plane neutral pressure. (g, h)* $T_{eo}$ *&* $T_{io}$*. (i) Line-averaged Zeff from a central (VB core) and an edge-viewing (VB edge) visible bremsstrahlung chord. (j) uncalibrated neutron rate by* $^{3}$*He detector.*

## 3.3. Role of EHM in Impurity Transport and Radiation Control

To uncover the physical mechanisms sustaining this stable, synergistic effect, we investigated the impurity transport and radiation distribution. The experimental evidence points to two interconnected core mechanisms. First, an EHM triggered by SBI provides a continuous outward particle transport channel for core impurity control; second, the synergistic injection actively reshapes the plasma's radiation profile, relocating radiation from the core to the plasma boundary.

The key to achieving stable high confinement lies in the effective control of core Ne content provided by the synergistic scheme. Figure 7 compares the pure Ne case (#93188, black) with two synergistic B+Ne discharges (#93191, orange; #93192, magenta), plotting key parameters as a function of the outer strike point temperature (Te@OSP). **Panel (a)** shows the Ne-II emission, measured by visible spectroscopy viewing the divertor target, while **panel (b)** displays a proxy for the upstream Ne content within the closed flux surfaces (Ne-IX/$n_e$) **[39]**. Coronal equilibrium indicates Ne-IX exists in the $T_e$ range of ~ 20 – 1000 eV, and the abundance fraction of $Ne^{8+}$ peaks at ~ 100 eV. A compelling trend emerges: the synergistic discharges, which exhibit higher Ne-II **[53]** radiation in the divertor (**panel a**), simultaneously maintain a lower and more controlled level of upstream Ne content (**panel b**). In contrast, the pure Ne discharge, despite having lower divertor Ne-II radiation, suffers from a continuous rise in upstream Ne as it cools, culminating in an unsustainable H-L transition, as shown by the $H_{98}$ collapse in **panel (c)**.

This result strongly suggests that the presence of B helps to confine Ne more effectively in the divertor region for radiation while simultaneously suppressing or expelling it from migrating upstream into the core. This stable $H_{98}$ response facilitates future feedback control systems, targeting the recovery of stored energy loss with finer or adaptive control of B and Ne injection, as reported in the literature **[37]**. The right panels (d–f) then provide the *mechanistic link* by showing cross-power spectrograms (cross-FFT) between Dα fluctuations at the upper divertor and AXUV fluctuations viewing the upper X-point region, isolating coherent fluctuation activity and identifying the EHM band as a persistent feature during SBI phases. Comparing #93188 (pure Ne) with #93191/#93192 (B+Ne), the EHM band is only observed when SBI is present, and it persists through the ELM-suppressed detached phase, demonstrating that the EHM coexists with Ne injection and detachment in the synergistic scenario.

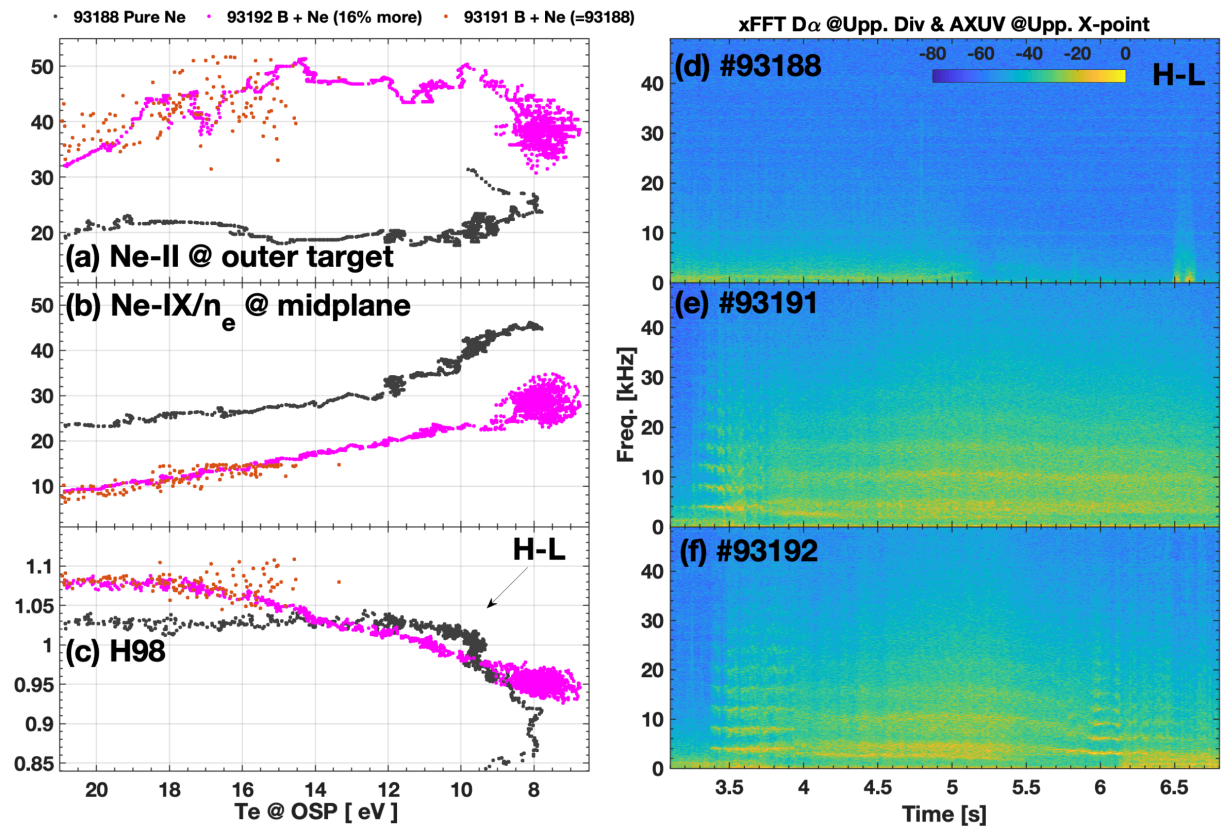


Figure 7 ***SBI-triggered EHM enables enhanced divertor Ne emissivity with reduced upstream Ne content proxy during synergistic B+Ne operation****. Left: Parametric comparison of pure-Ne discharge #93188 (black) and synergistic B+Ne discharges #93191 (orange) and #93192 (magenta) plotted versus outer strike-point temperature $T_e$ at the outer strike point (OSP): (a) Ne-II emission at the outer target (divertor radiation proxy), (b) Ne-IX/$n_e$ at the midplane (upstream/core-near proxy), and (c) confinement factor $H_{98}$. Right: cross-power spectrograms (cross-FFT) between Dα fluctuations at the upper divertor and AXUV radiation fluctuations viewing the upper X-point region for (d) #93188, (e) #93191, and (f) #93192; a persistent EHM band is observed only when SBI is applied, and remains during the ELM-suppressed detached phase of #93192.*

Because full profile-based transport inference is not available for all discharges, the impurity exhaust capability is additionally quantified using compact "effective" relaxation metrics

(Figure 8), while explicitly acknowledging that line-integrated proxies can be influenced by emissivity and charge-state balance. First, an effective Ne removal time is estimated from the decay of the Ne-IX/$n_e$ proxy following valve shutoff, yielding a modest but measurable reduction of the effective decay time in the EHM/ELM-suppressed case (#93194 $\tau_{Ne} \approx 2394$ms) relative to an ELMing case without EHM (#93187 $\tau_{Ne} \approx 2696$ms). This comparison is conservative because #93187 contains ELMs (**panel** g), which would normally provide intermittent flushing; therefore, observing a slightly longer effective decay time in the ELMing case implies that the EHM/ELM-suppressed phase is not transport-starved and is consistent with a continuous outward exhaust channel when ELM flushing is absent. To reduce the possibility that changes in atomic physics dominate the Ne-IX proxy, we also checked that pedestal $T_e$ (ECE at $\rho \sim 0.8$) variation is negligible.

Second, an effective high-Z removal time is extracted from W-UTA relaxation following impulsive UFO events, where the fit is started after the emission peak to exclude the source phase. The W-UTA signal is then fitted with a single-exponential-plus-offset form, $y = A\exp(-(t - t_s)/\tau_W) + C$, yielding $\tau_W$ as the effective high-Z removal timescale for that event. In Figure 8 (a–b), discharge #93186 shows a UFO event followed by a W-UTA decay with $\tau_W \sim 107$ ms, while in Figure 8 (c–d), discharge #93191 shows a UFO event with a faster W-UTA decay, $\tau_W \sim 70$ ms. The two discharges are executed with similar global settings (e.g., plasma shape and comparable heating/programming), and both are in attached conditions (target Te ~ 20eV) during the respective UFO windows; however, the edge regime differs (#93186 is ELMing/mitigated whereas #93191 is EHM/ELM-absent), so we interpret the different $\tau_W$ values as an edge-regime-dependent effective W removal time. This difference is consistent with enhanced impurity exhaust in the EHM case, but we avoid claiming a unique transport coefficient because we have limited numbers of impulsive events and because emissivity/charge-state effects can contribute to the apparent W-UTA decay.

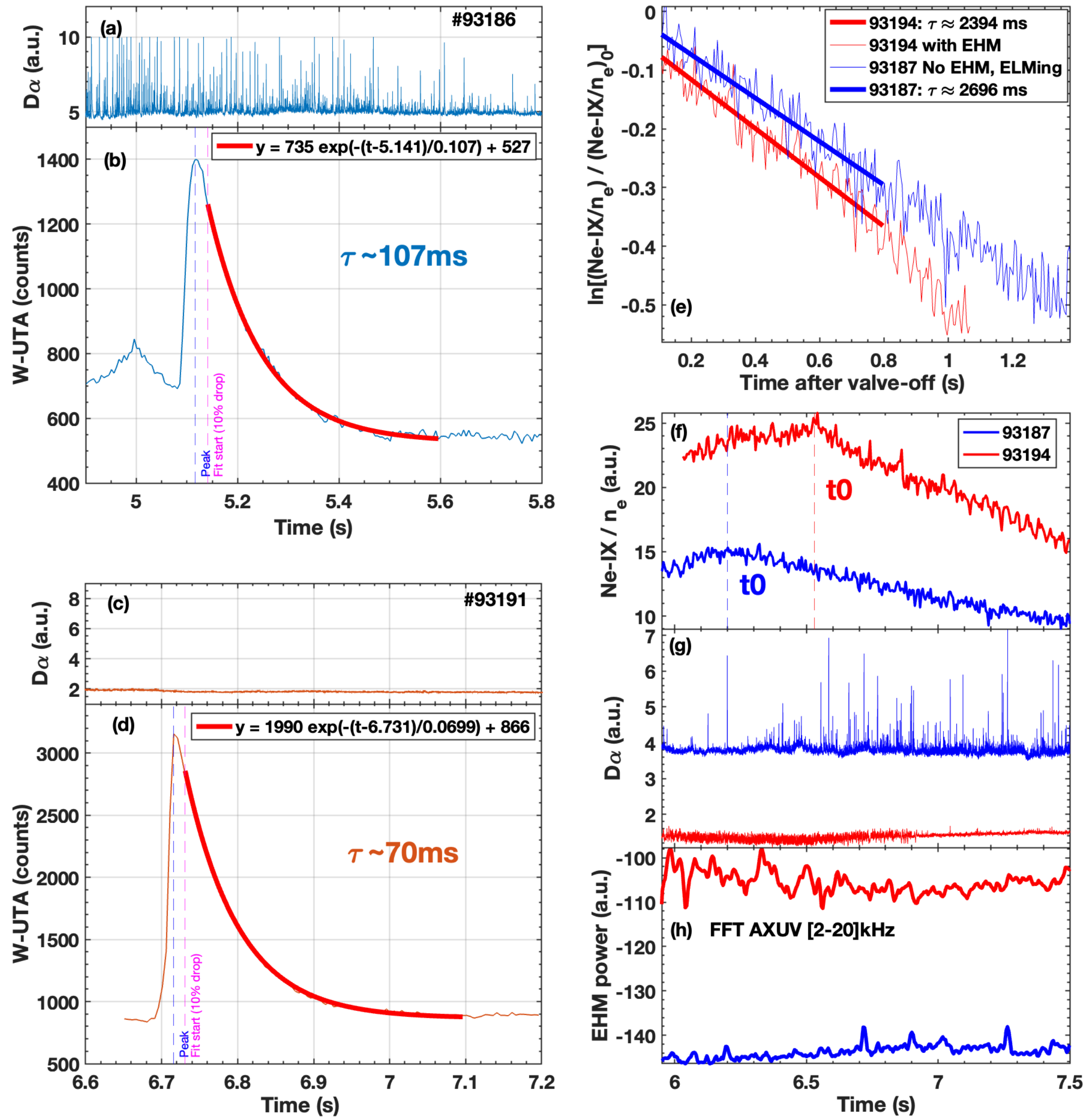


Figure 8 ***Proxy-based effective impurity removal times with and without EHM and ELMs.*** *Left: Examples of W-UTA relaxation following an impulsive 'UFO' event for (a–b) #93186 and (c–d) #93191, where the fit is started after the peak and the decay is fitted with a single exponential to extract an effective W-UTA decay time ($\tau_W$). Right: (e) semilog plot of the Ne-IX/ne proxy after valve-off for an EHM/ELM-suppressed discharge (#93194) and an ELMing discharge without EHM (#93187), showing approximately linear semilog behavior over the selected fitting windows and yielding an effective neon-proxy decay time ($\tau_{Ne}$); (f–h) accompanying time traces (Ne-IX/ne, Dα, and EHM power) are shown to document the edge regime.*

A sequence-reversal experiment is used to separate "screening" from active impurity reduction and to demonstrate simultaneous radiation reshaping. In discharge #93194, Ne was injected first, followed by B powder. **Panel** (a & c) in Figure 9 shows that after Ne injection at t ~ 3.5s, and then after SBI started at 4s, ELMs were suppressed and an EHM was initiated at t ~ 4.2s.

The EHM signal is quantified by integrating the fluctuation power of an AXUV chord in the 2–20 kHz band (shown as 'EHM power'). During the Ne-only phase with suppressed ELM flushing, impurity accumulation (both seeded Ne and intrinsic high-Z species) is expected to be a key risk as #93185 and #93188: once ELMs are removed, the plasma can no longer rely on ELM losses to expel impurities, so sustained outward transport is required to avoid progressive core contamination and radiative degradation. Figure 9 shows that after SBI onset, the EHM power rises and remains present through the energy detached ($T_e$@OSP < 10eV) and ELM-suppressed phase spanning ~4.5 - 6.6 s (bounded by the vertical dashed lines), while the Ne proxy (Ne-IX/$n_e$) and the volume-averaged Molybdenum content, $C_{Mo}$, stop rising and later decrease, and the estimated $C_W$ is rapidly reduced and remains controlled. The tungsten signal can decrease simply because the divertor tungsten source decreases as the target temperature is reduced, and therefore a reduction of $C_W$ during Ne-driven cooling cannot by itself demonstrate 'tungsten pump-out'. Mo, as a complementary high-Z indicator (Figure 9 (e)), is associated with midplane plasma–wall interaction rather than divertor-target sputtering, and $C_{Mo}$ decreases during the EHM phase in #93194 while it ramps up in the non-EHM reference #93188. Taken together, these time-correlated trends are consistent with the interpretation that SBI-triggered EHM provides a continuous outward impurity transport channel that can prevent impurity accumulation when ELM flushing is absent. This experiment clearly distinguishes between impurity "screening" (preventing entry) and "pump-out" (active expulsion). Since the core impurities were already present and subsequently reduced after the EHM appeared, this suggests that the EHM provided an active outward transport, or "pump-out," mechanism. Further supporting this, Figure 9 (c) shows that in discharge #93193 (with early SBI), the rise of the Ne proxy was much slower than in #93194 (late SBI), indicating that an early, persistent EHM provided both screening and pump-out, which is key to achieving the steady-state impurity control necessary for stationary operation.

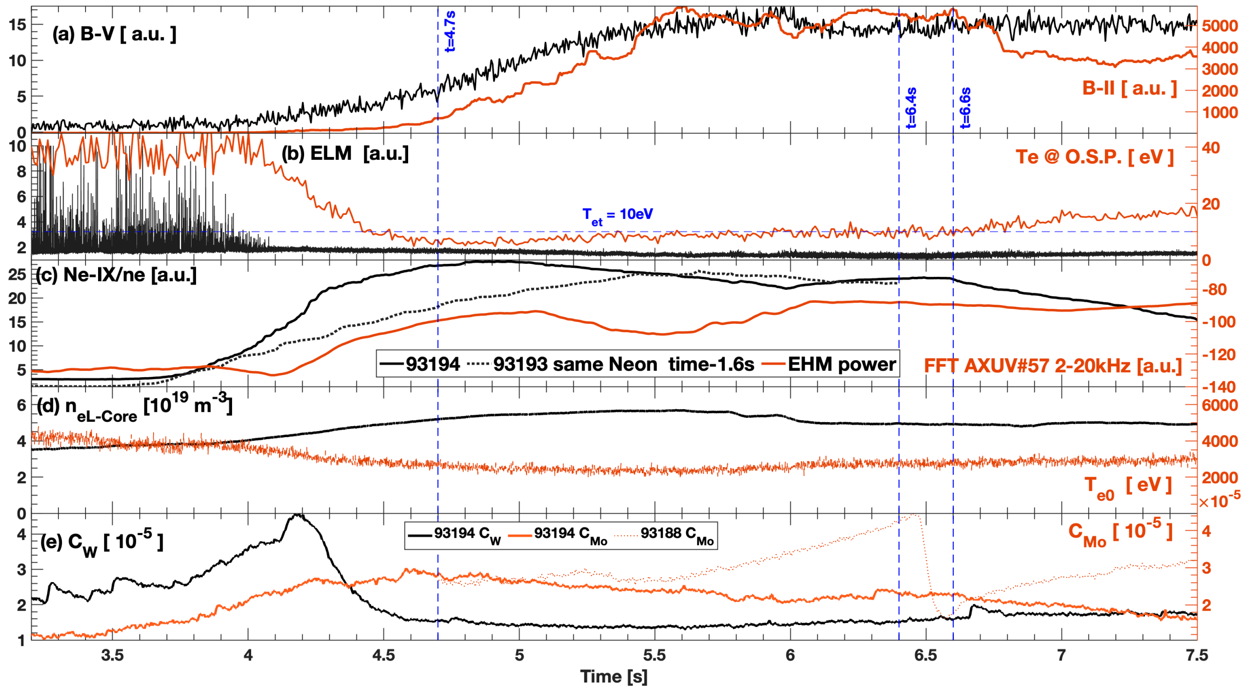


Figure 9 ***Evidence of EHM onset and subsequent multi-impurity control in discharge #93194***. *(a) B-V (black) and B-II (orange) emission indicating the SBI phase evolution. (b) ELM indicator and outer strike-point temperature $T_e$ @OSP, with the blue dashed horizontal line marking $T_e$ @OSP = 10 eV as a reference for the onset/maintenance of a low-temperature divertor condition. (c) Ne-IX/$n_e$ proxy (solid, #93194) compared with 93193 (dotted, time-shifted by -1.6 s to align the Ne injection timing), overlaid with the EHM intensity metric ('EHM power') obtained by integrating the AXUV fluctuation power in the 2–20 kHz band. (d) Core line-averaged density and a core temperature. (e) Volume-averaged W and Mo concentrations $C_W$ and $C_{Mo}$ (with #93188 $C_{Mo}$ shown for comparison). The first two vertical dashed lines mark the time slices for the SXR tomography; the last one indicates termination of Ne injection.*

The radiation redistribution is quantified by AXUV and independently confirmed by SXR tomography, as detailed in Figure 10. **Panel (a)** shows the time evolution of the AXUV (Figure 1) line-integrated radiation power. The four vertical dashed lines represent the time slices for detailed comparison in **panels (b & c)**. Initially, Ne injection (from t=3.5s to 4.2s, black squares in **panel (c)**) increased the radiation in both the core (Ch# 30-48) and the edge (Ch# 55-63), but with a larger relative increase in the core (130-220%) compared to the edge (100-180%). However, after B was added, and B & Ne injection continued (from t ~ 4.7s to 6.4s, purple stars in **panel (c)**), the situation reversed: the core channel (Ch# 30-42) radiation was reduced by ~15%, while the edge channels near the X-point (Ch# 59-61) exhibited an increase of ~15%, indicating a shift of radiated power from the hot region toward the boundary.

The 2D tomographic profiles from the soft X-ray (SXR) arrays **[54]**, shown in **panels (d-f)**, provide corroborating evidence, a more geometry-robust confirmation of reduced core radiation. The SXR diagnostic is insensitive to photons with energy <1keV and thus primarily reflects radiation from the hotter region inside the pedestal. The SXR reduction from t=4.7s to t=6.4s is strongest in the core (~30%, peak around $\rho\sim0$) and decreases toward the outer radii (to ~12%

near the edge of the SXR sensitivity region), consistent with the **core reduction** inferred from AXUV.

Since fixed-view AXUV chords—especially those intersecting the X-point region—can be sensitive to radiation weight and modest equilibrium shifts, an EFIT-based geometry check using EFIT reconstructions at representative times (4.7 s and 6.4 s) shows that the upstream separatrix position is essentially unchanged while the X-point shifts only modestly. AXUV Ch# 6 (Figure 1), which traverses the upstream SOL and is approximately tangential to the upstream separatrix, exhibits a clear increase over 4.7–6.4 s, consistent with an increase of edge/SOL radiation in this interval. In addition, divertor-visible B emission (B-II) increases during the same interval (Figure 9 a), supporting the idea that the increase in edge/SOL radiation is not solely an artifact of equilibrium variation. B-II emission increases significantly due to (i) Boron distribution in plasma and on targets with a continuous constant injection has not reached a balance; (ii) Neon induced low temperature near the target boosts the Boron radiation, which is consistent with B-II decay as the target Te ramps up after t ~ 6.6s due to the Neon injection termination.

Taken together, the cross-FFT identification of a persistent EHM, the proxy-based relaxation times, and the sequence-reversal radiation/impurity evolution support the conclusion that SBI-triggered EHM provides a continuous outward exhaust channel that enables sustained neon seeding and energy detachment without the impurity accumulation that limits pure-Ne operation.

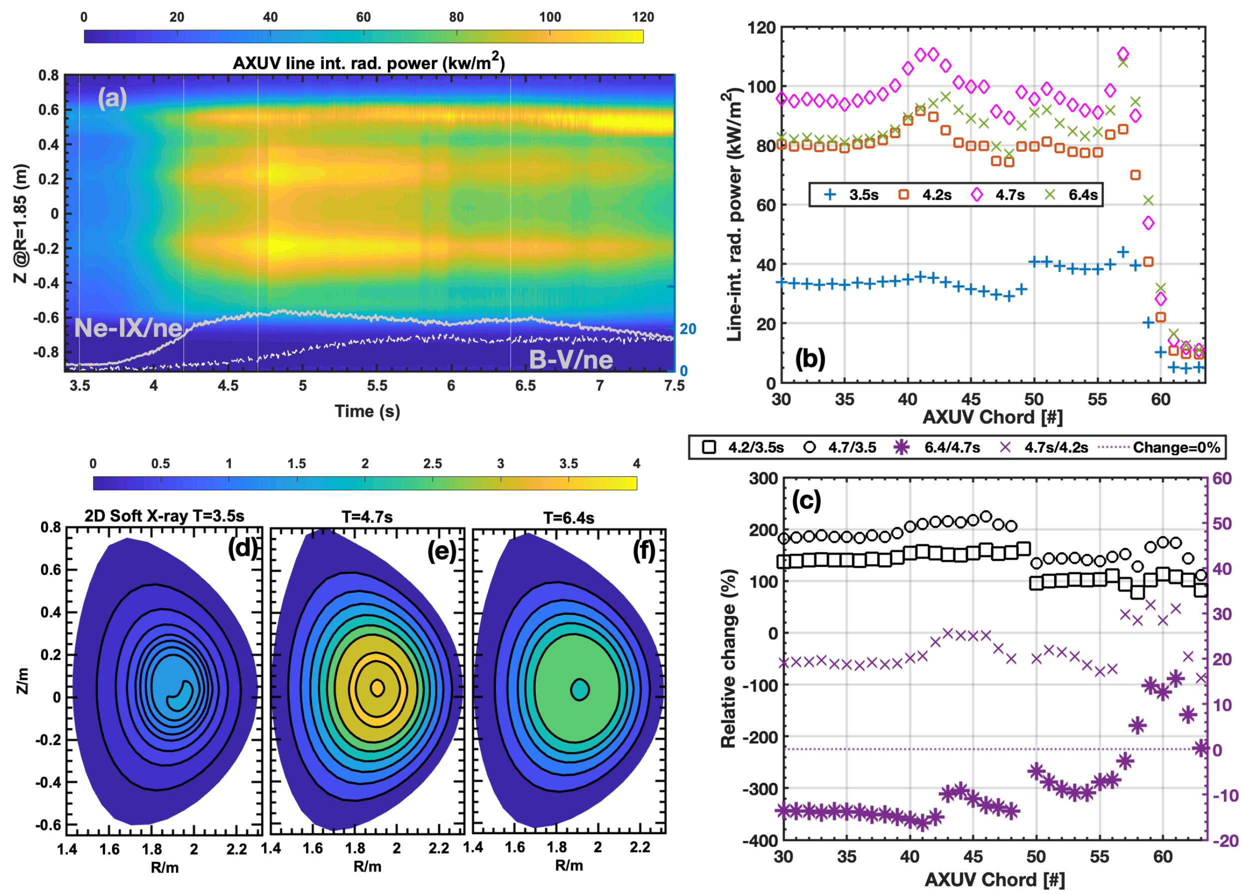


Figure 10 ***Synergistic B+Ne injection reshapes the radiation profile from core to edge in discharge #93194.*** *(a) Time evolution of the AXUV line-integrated radiation profile, with vertical white lines indicating time slices. (b) AXUV power of all chords in the upper part for the four time slices. (c) Relative change of the radiation profile between time slices. (d), (e), (f) are 2D reconstructions of the soft X-ray emissivity, showing a hollowing of the core emission after SBI.*

## 3.4 Complementary Radiative Cooling Effects of the B+Ne Mixture

Beyond altering transport via the EHM, a second synergistic mechanism is the optimization of radiative cooling efficiency by tuning the B:Ne mixture. To investigate this, we compare discharge #93192 (lower B, higher Ne rate) with #93193 (higher B, lower Ne rate). While both achieved ELM suppression, #93193 did not reach the same deeply detached state (8 eV versus 5.5 eV) due to its lower Ne rate, which is a more effective radiator in the hotter upstream SOL-pedestal regions.

To facilitate a physically meaningful comparison, Figure 11 plots key parameters as a function of the outer strike point temperature ($T_e$@OSP). This approach directly links the divertor condition ($T_e$@OSP) to the corresponding upstream plasma state. In the crucial overlapping operational window of 8 eV < $T_e$@OSP < 12 eV, a trend emerges. The high-B discharge (#93193, magenta) exhibited significantly lower core Ne content (Ne-IX proxy, **panel (a)**) and consequently lower core radiation (AXUV core, **panel (c)**) compared to the high-Ne discharge (#93192, green).

This experimental result is a compelling manifestation of the non-coronal equilibrium (NCE) atomic physics illustrated in Figure 2. In this low-temperature divertor regime, B's NCE radiation efficiency is strongly enhanced. The increased B in #93193 thus effectively substitutes for a portion of the Ne in providing radiative cooling. This allows a similar level of cooling to be achieved with less Ne, directly reducing core contamination. While based on a direct comparison of two discharges, the strong consistency between this observation and fundamental atomic physics principles suggests that the B:Ne ratio can be used as a tool to actively optimize the radiation profile, minimizing core radiation beyond what is achievable by transport effects alone.

However, the higher-B/lower-Ne discharge #93193 also exhibits a modest reduction in global confinement compared to #93192 over much of the evolution. The reduction is evident even before the Ne-seeding transition, suggesting a confinement cost associated with the stronger SBI operating point. In the deep energy-detached regime ( $T_e$@OSP $\lesssim$ 8.5 eV), the $H_{98}$ in #93192 and #93193 become comparable; this convergence should be interpreted as a result of the specific actuator settings rather than a fundamental limit.

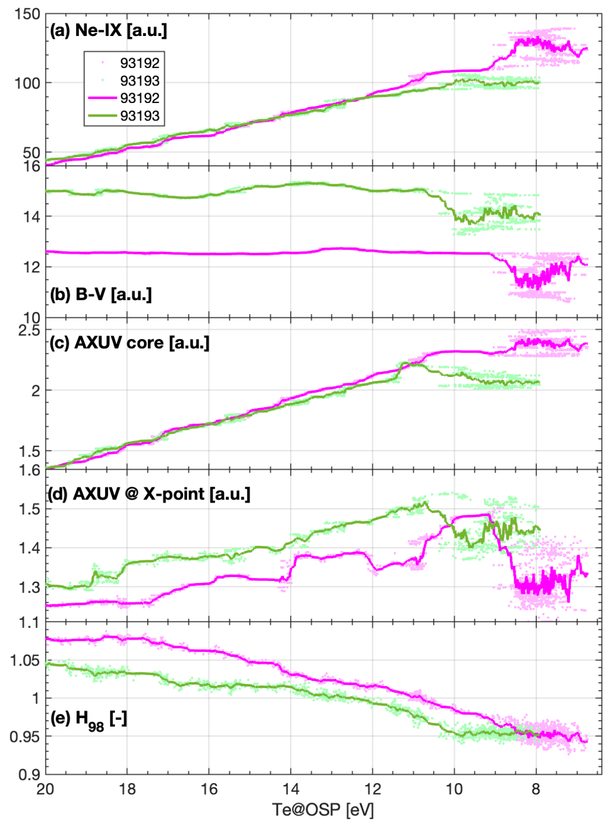


Figure 11 ***Comparison of discharges with different B:Ne ratios (#93192 vs #93193) plotted versus $T_e$@OSP.*** *(a) Ne-IX emission (proxy for upstream Ne); (b) B-V emission (proxy for SBI); (c) Core AXUV radiation; (d) AXUV radiation around X-point; (e) $H_{98}$ factor. In the overlapping $T_e$@OSP range of 8-12 eV, the higher-B, lower-Ne discharge (#93193, green) shows lower core Ne emission and core radiation for a given divertor temperature, at nearly identical confinement.*

# 4. Discussion

The experimental results support the concept of a synergistic B+Ne scenario, which operates via a twofold physics mechanism. First, B and Ne act as complementary radiators, with their effectiveness enhanced under the non-coronal equilibrium conditions of the divertor (Figure 2). Second, and most critically, SBI triggers a persistent EHM, which drives a continuous outward particle flux essential for impurity exhaust. This EHM-driven transport prevents the accumulation of Ne in the core and fundamentally changes the transport regime of the plasma edge to one that is compatible with robust impurity seeding.

The excitation of the EHM is likely understood to be a consequence of the modified edge plasma state rather than a unique intrinsic property of the boron atom itself. The injection acts as a localized actuator, introducing a particle and radiation source near the X-point, which modifies density gradients and alters local resistivity. Two primary drive mechanisms are proposed: (1) the localized density perturbation from powder ablation breaking poloidal symmetry to excite a Geodesic Acoustic Mode (GAM)-like instability [27], or (2) a radiative condensation instability driven by the negative temperature dependence of the impurity cooling rate ($dL_z/dT_e < 0$) [55]. Boron is particularly effective here because its non-coronal radiation efficiency peaks within the specific temperature range of the EAST pedestal and X-point region, maximizing the drive for these instabilities.

This dual-mechanism synergy provides a substantial advantage over pure Ne seeding scenarios explored on other machines[11,56,57]. While experiments on JET and DIII-D have achieved detached or ELM-suppressed states with Ne, they often report a narrow operational window, precariously balanced against core radiation limits or H-L back-transitions[7,8,11,13,14]. The B+Ne scenario presented here breaks that paradigm. The EHM, actively driven by SBI, provides a reliable, continuous impurity exhaust channel that is absent in pure Ne scenarios once ELMs are suppressed. This allows for stable operation in a much wider parameter space, as demonstrated by the prevention of the H-L transition compared to the pure Ne case in Figure 4, and enables control of core impurities even after they have entered the plasma and stabilized the pedestal, as shown in the sequence-reversal experiment of Figure 9.

Interestingly, the underlying physics of this solution bears a strong resemblance to the ELM-free EDA H-mode explored on ASDEX Upgrade with Ar seeding [2,5]. In the EDA H-mode, a naturally occurring Quasi-Coherent Mode (QCM), much like our EHM, provides the necessary particle transport to prevent impurity accumulation. The injection of Ar in that scenario primarily serves to reduce the pedestal pressure to maintain the plasma within the stable EDA regime. Our approach can be considered an 'engineered' analogue to this physics: where a QCM is not naturally present, we use SBI as an actuator to reliably trigger an EHM, thereby creating the necessary transport conditions to enable stable operation with a radiative impurity. This positions our work within a more universal framework for advanced tokamak scenarios, based on the principle of replacing intermittent ELM transport with a continuous, benign edge mode.

This insight also opens a promising avenue for future research: a synergistic B+Ar scenario. As reported from ASDEX Upgrade, Ar exhibits a significantly higher divertor enrichment than Ne, meaning less impurity is required in the core for the same divertor radiation [6]. However, Ar's higher atomic number also makes it a more dangerous core radiator if it does accumulate. A B+Ar scheme could be highly advantageous, combining the superior radiative and retention properties of Ar with the EHM-driven "safety valve" for impurity control provided by SBI.

Finally, this work provides a practical demonstration of an integrated scenario with significant implications for ITER. The observed EHM is analogous to the QH-mode regimes[1], while traditional EHOs are driven by rotational shear (kink-peeling), the Boron-induced EHM is likely driven by collisionality and radiation gradients. Given that real-time powder injection is an increasingly mature technology [36] and SBI is already being considered for ITER for other purposes (e.g., oxygen gettering) [23], our results show this same system could be a primary actuator for a robust, integrated core-edge solution.

# 5. Summary and Outlook

This paper has presented the first successful demonstration of simultaneous ELM suppression and partial divertor detachment through the synergistic use of SBI and Ne gas injection in the EAST tokamak. The solution overcomes the limitations of using either impurity alone by employing a dual synergistic mechanism. The combined injection of B and Ne establishes a stationary, ELM-suppressed H-mode with an energy-detached outer divertor ($T_e$ < 10 eV), good confinement ($H_{98}$ ~ 1), and a significantly expanded operational window compared to pure Ne seeding. The success of the scenario is underpinned by two key physics mechanisms acting in concert: (1) SBI reliably triggers a persistent EHM. This mode provides a continuous outward particle transport channel that is critical for preventing core Ne accumulation, accompanied by high-Z impurity pinch, a fundamental problem in pure Ne and Ar seeding scenarios; (2) The B+Ne mixture leverages the complementary, non-coronal equilibrium radiation characteristics of the two species. Experimental evidence shows that an optimized B:Ne ratio can reduce core radiation by substituting a portion of the Ne with B for low-temperature cooling. This scenario leads to favorable radiation redistribution, including a ~15% reduction in AXUV core chords in the sequence-reversal discharge after SBI/EHM onset, with a consistent ~12-30% reduction in SXR core emissivity. Although line-integrated $Z_{eff}$ increases during impurity seeding, the neutron rate does not decrease in the demonstrated stationary phase, suggesting that any dilution is not performance-limiting in the demonstrated stationary phase. Quantifying core dilution more definitively requires dedicated profile-resolved measurements and analysis.

These results demonstrate a practical pathway toward integrated core-edge operation relevant to ITER by combining an SBI-triggered EHM with active tailoring of the radiated-power distribution using mixed impurities. Future work will map the operational window and portability by scanning injection location (X-point vs upstream/midplane), duty cycle, and powder species (B/BN/Li)[16,58,59], while measuring the mode structure to clarify whether the observed EHM is best interpreted as an impurity-driven low-n X-point mode, a GAM-like response, or a QH/EHO-like branch[1]. In parallel, predictive edge/SOL modeling, e.g., SOLPS-ITER, Hermes-3 with localized impurity sources and non-coronal radiation will be pursued, along with extension to other radiators (e.g., Ar) and development of real-time feedback control that regulates both transport and radiation. Finally, reactor-relevant open issues—boron inventory buildup, migration to shadowed regions, and potential tritium co-deposition—must be quantified and mitigated with integrated fuel-recovery and material-lifecycle strategies.

## Acknowledgments

This work was supported by the U.S. Department of Energy under contract number DE-AC02-09CH11466. The United States Government retains a non-exclusive, paid-up, irrevocable, worldwide license to publish or reproduce the published form of this manuscript, or allow others to do so, for United States Government purposes. The authors would like to thank the EAST team for their support of the experiments. This work was also supported in part by the National Key Research and Development Program of China (2024YEF03000200, 2024YFE03270700, 2022YFE03180400, 2022YFE03040003, 2022YFE03100003, 2022YFE03130004, 2024YFE03020003, 2024YFE03250300) and the National Natural Science Foundation of China (12505247, 12305250, 12205336, 12475208, 12475207). The data that support the findings of this study are available from the corresponding authors upon reasonable request. Raw data were generated at the EAST facility.

# Reference

[1] M. E. Fenstermacher, L. R. Baylor, E. de la Luna, M. G. Dunne, G. T. A. Huijsmans, A. Kirk, F. M. Laggner, T. H. Osborne, C. Paz-Soldan, S. Saarelma *et al.*, Nuclear Fusion 65, 053001 (**2025**). Progress in pedestal and edge physics: Chapter 3 of the special issue: on the path to tokamak burning plasma operation; https://doi.org/10.1088/1741-4326/adb1f3

[2] K. Krieger, S. Brezinsek, J. W. Coenen, H. Frerichs, A. Kallenbach, A. W. Leonard, T. Loarer, S. Ratynskaia, N. Vianello, N. Asakura *et al.*, Nuclear Fusion 65, 043001 (**2025**). Scrape-off layer and divertor physics: Chapter 5 of the special issue: on the path to tokamak burning plasma operation; https://doi.org/10.1088/1741-4326/adaf42

[3] R. A. Pitts, A. Loarte, T. Wauters, M. Dubrov, Y. Gribov, F. Köchl, A. Pshenov, Y. Zhang, J. Artola, X. Bonnin *et al.*, Nucl Mater Energy 42, 101854 (**2025**) 101854. Plasma-wall interaction impact of the ITER re-baseline; https://doi.org/10.1016/j.nme.2024.101854

[4] R. A. Pitts, X. Bonnin, F. Escourbiac, H. Frerichs, J. P. Gunn, T. Hirai, A. S. Kukushkin, E. Kaveeva, M. A. Miller, D. Moulton *et al.*, Nucl Mater Energy 20, 100696 (**2019**) 100696. Physics basis for the first ITER tungsten divertor; https://doi.org/10.1016/j.nme.2019.100696

[5] A. Kallenbach, M. Bernert, P. David, M. G. Dunne, R. Dux, E. Fable, R. Fischer, L. Gil, T. Görler, F. Janky *et al.*, Nuclear Fusion 61 (**2020**) 016002. Developments towards an ELM-free pedestal radiative cooling scenario using noble gas seeding in ASDEX Upgrade; https://doi.org/10.1088/1741-4326/abbba0

[6] A. Kallenbach, M. Bernert, R. Dux, L. Casali, T. Eich, L. Giannone, A. Herrmann, R. McDermott, A. Mlynek, H. W. Muller *et al.*, Plasma Physics and Controlled Fusion 55 (**2013**) 124041. Impurity seeding for tokamak power exhaust: from present devices via ITER to DEMO; https://doi.org/10.1088/0741-3335/55/12/124041

[7] D. G. Wu, L. Wang, H. Q. Wang, A. M. Garofalo, X. Z. Gong, S. Ding, Y. F. Wang, H. Lan, N. Yan, J. McClenaghan *et al.*, Nuclear Fusion 64 (**2024**) 086042. Compatibility of divertor detachment and ELM suppression in DIII-D high-βp plasmas with ITER-similar shape; https://doi.org/10.1088/1741-4326/ad5852

[8] C. Giroud, I. S. Carvalho, S. Brezinsek, A. Huber, D. Keeling, J. Mailloux, R. A. Pitts, E. Lerche, R. Henriques, J. Hillesheim *et al.*, Nuclear Fusion 64 (**2024**) 106062. The core–edge integrated neon-seeded scenario in deuterium–tritium at JET; https://doi.org/10.1088/1741-4326/ad69a2

[9] K. Li, X. Lin, Z. Yang, Q. Yang, G. Xu, L. Meng, Y. Wang, H. Lan, B. Zhang, L. Xu *et al.*, Nuclear Fusion 63 (**2023**) 026025. Compatibility of large ELM control and stable partial detachment with neon/argon seeding in EAST; https://doi.org/10.1088/1741-4326/acae36

[10] S. Gabriellini, L. Garzotti, V. K. Zotta, C. Bourdelle, F. J. Casson, J. Citrin, D. Frigione, R. Gatto, C. Giroud, F. Koechl *et al.*, Nuclear Fusion 63 (**2023**) 086025. Neon seeding effects on two high-performance baseline plasmas on the Joint European Torus; https://doi.org/10.1088/1741-4326/ace2d7

[11] A. Huber, M. Wischmeier, M. Bernert, S. Wiesen, S. Glöggler, S. Aleiferis, S. Brezinsek, G. Calabro, P. Carvalho, V. Huber *et al.*, Phys. Scr. T171 (**2020**) 014055. Peculiarity of highly

radiating multi-impurity seeded H-mode plasmas on JET with ITER-like wall; https://doi.org/10.1088/1402-4896/ab5753

[12] E. R. Solano, N. Vianello, E. Delabie, J. C. Hillesheim, P. Buratti, D. Réfy, I. Balboa, A. Boboc, R. Coelho, B. Sieglin *et al.*, Nuclear Fusion 57 (**2016**) 022021. Axisymmetric oscillations at L–H transitions in JET: M-mode; https://doi.org/10.1088/0029-5515/57/2/022021

[13] S. Glöggler, M. Wischmeier, E. Fable, E. R. Solano, M. Sertoli, M. Bernert, G. Calabrò, M. Chernyshova, A. Huber, E. Kowalska-Strzęciwilk *et al.*, Nuclear Fusion 59 (**2019**) 126031. Characterisation of highly radiating neon seeded plasmas in JET-ILW; https://doi.org/10.1088/1741-4326/ab3f7a

[14] H. Q. Wang, L. Wang, S. Ding, A. M. Garofalo, X. Z. Gong, D. Eldon, H. Y. Guo, A. W. Leonard, A. W. Hyatt, J. P. Qian *et al.*, Phys Plasmas 28 (**2021**) 052507. Observation of fully detached divertor integrated with improved core confinement for tokamak fusion plasmas; https://doi.org/10.1063/5.0048428

[15] M. Bernert, M. Wischmeier, A. Huber, F. Reimold, B. Lipschultz, C. Lowry, S. Brezinsek, R. Dux, T. Eich, A. Kallenbach *et al.*, Nucl Mater Energy 12, 111 (**2017**) 111. Power exhaust by SOL and pedestal radiation at ASDEX Upgrade and JET; https://doi.org/10.1016/j.nme.2016.12.029

[16] H. Schamis, E. P. Gilson, H. Lee, R. Maingi, S. Kim, J. A. Snipes, S. Yang, A. Bortolon, J. Jang, B. Kim *et al.*, Nuclear Fusion 65 (**2025**) 086037. Wall conditioning effects of boron powder injection in KSTAR with a tungsten divertor; https://doi.org/10.1088/1741-4326/adf123

[17] K. Krieger, M. Balden, A. Bortolon, R. Dux, M. Griener, K. Hegele, F. Laggner, V. Rohde, and W. R. Wampler, Nucl Mater Energy 34 (**2023**) 101374. Wall conditioning effects and boron migration during boron powder injection in ASDEX Upgrade; https://doi.org/10.1016/j.nme.2023.101374

[18] G. Bodner, A. Gallo, A. Diallo, R. Lunsford, P. Moreau, A. Nagy, F. P. Pellissier, C. Guillemaut, J. P. Gunn, C. Bourdelle *et al.*, Nuclear Fusion 62 (**2022**) 086020. Initial results from boron powder injection experiments in WEST lower single null L-mode plasmas; https://doi.org/10.1088/1741-4326/ac70ea

[19] F. Effenberg, A. Bortolon, L. Casali, R. Nazikian, I. Bykov, F. Scotti, H. Q. Wang, M. E. Fenstermacher, R. Lunsford, A. Nagy *et al.*, Nuclear Fusion 62 (**2022**) 106015. Mitigation of plasma–wall interactions with low-Z powders in DIII-D high confinement plasmas; https://doi.org/10.1088/1741-4326/ac899d

[20] R. Lunsford, V. Rohde, A. Bortolon, R. Dux, A. Herrmann, A. Kallenbach, R. M. McDermott, P. David, A. Drenik, F. Laggner *et al.*, Nuclear Fusion 59 (**2019**) 126034. Active conditioning of ASDEX Upgrade tungsten plasma-facing components and discharge enhancement through boron and boron nitride particulate injection; https://doi.org/10.1088/1741-4326/ab4095

[21] F. Nespoli, N. Ashikawa, E. P. Gilson, R. Lunsford, S. Masuzaki, M. Shoji, T. Oishi, C. Suzuki, A. Nagy, A. Mollen *et al.*, Nucl Mater Energy 25 (**2020**) 100842. First impurity powder injection experiments in LHD; https://doi.org/10.1016/j.nme.2020.100842

[22] J. A. Snipes, L. R. Baylor, A. Bortolon, F. Effenberg, E. P. Gilson, A. Loarte, R. Lunsford, R. Maingi, S. Meitner, F. Nespoli *et al.*, Nucl Mater Energy 41, 101809 (**2024**) 101809. Initial design concepts for solid boron injection in ITER; https://doi.org/10.1016/j.nme.2024.101809

[23] A. Loarte, R. Pitts, T. Wauters, I. Nunes, F. Köchl, A. Polevoi, S. Kim, M. Lehnen, J. Artola, and L. Chen, Initial evaluations in support of the new ITER baseline and Research Plan, 2024, Technical Report No. ITR-24-004, https://www.iter.org/sites/default/files/media/2024-04/itr-24-004-baseline-ok.pdf.

[24] Z. Sun, R. Maingi, A. Diallo, W. Xu, Y. Z. Qian, K. Tritz, Y. Ye, C. L. Li, Z. Xu, Y. F. Wang *et al.*, Phys Plasmas 28, 082512 (**2021**) 082512. Enhancement of edge turbulence concomitant with ELM suppression during boron powder injection in EAST; https://doi.org/10.1063/5.0058809

[25] Z. Sun, A. Diallo, R. Maingi, Y. Z. Qian, K. Tritz, Y. F. Wang, Y. M. Wang, A. Bortolon, A. Nagy, L. Zhang *et al.*, Nuclear Fusion 61, 014002 (**2021**) 014002. Suppression of edge localized modes with real-time boron injection using the tungsten divertor in EAST; https://doi.org/10.1088/1741-4326/abc763

[26] E. P. Gilson, H. H. Lee, A. Bortolon, W. Choe, A. Diallo, S. H. Hong, H. M. Lee, J. Lee, R. Maingi, D. K. Mansfield *et al.*, Nucl Mater Energy 28 (**2021**) 101043. Wall conditioning and ELM mitigation with boron nitride powder injection in KSTAR; https://doi.org/10.1016/j.nme.2021.101043

[27] A. Diallo, Preprint: 2020 IAEA Fusion Energy Conf. (**2021**). First observation of ELM suppression without confinement degradation due to geodesic acoustic mode (GAM)-like mode triggered by boron powder injection 28th IAEA Fusion Energy Conf. (FEC 2020) (Virtual Event, 10–15 May 2021) (available at:

https://nucleus.iaea.org/sites/fusionportal/Shared%20Documents/FEC%202020/fec2020-synopsis/Synopsis1167.pdf);

[28] R. Maingi, J. S. Hu, Z. Sun, A. Diallo, K. Tritz, Y. Z. Qian, W. Xu, G. Z. Zuo, C. L. Li, M. Huang *et al.*, J Fusion Energ 39, 429 (**2020**). ELM Suppression by Boron Powder Injection and Comparison with Lithium Powder Injection on EAST; https://doi.org/10.1007/s10894-020-00256-3

[29] A. A. Mavrin, J Fusion Energ 36, 161 (**2017**) 161. Radiative Cooling Rates for Low-Z Impurities in Non-coronal Equilibrium State; https://doi.org/10.1007/s10894-017-0136-z

[30] S. O. Makarov, D. P. Coster, T. Gleiter, D. Brida, M. Muraca, R. Dux, P. David, B. Kurzan, X. Bonnin, and M. O'Mullane, Contributions to Plasma Physics 64 (**2024**). First SOLPS-ITER simulations of ASDEX Upgrade partially detached H-mode with boron impurity: The missing radiation at the outer strike-point region; https://doi.org/10.1002/ctpp.202300139

[31] F. Effenberg, K. Schmid, F. Nespoli, A. Bortolon, Y. Feng, B. A. Grierson, J. D. Lore, R. Maingi, and D. L. Rudakov, Nucl Mater Energy 42 (**2025**) 101832. Integrated modeling of boron powder injection for real-time plasma-facing component conditioning; https://doi.org/10.1016/j.nme.2024.101832

[32] P. C. Stangeby, E. A. Unterberg, J. W. Davis, T. Abrams, A. Bortolon, I. Bykov, D. Donovan, H. Y. Guo, R. Kolasinski, A. W. Leonard *et al.*, Plasma Physics and Controlled Fusion 64 (**2022**). Developing solid-surface plasma facing components for pilot plants and reactors with replenishable wall claddings and continuous surface conditioning. Part A: concepts and questions; https://doi.org/10.1088/1361-6587/ac5a7c

[33] K. Schmid and T. Wauters, Nucl Mater Energy 41 (**2024**) 101789. Full W ITER: Assessment of expected W erosion and implications of boronization on fuel retention; https://doi.org/10.1016/j.nme.2024.101789

[34] B. N. Wan, X. Z. Gong, Y. Liang, N. Xiang, G. S. Xu, Y. Sun, L. Wang, J. P. Qian, H. Q. Liu, B. Zhang *et al.*, Nuclear Fusion 62, 042010 (**2022**) 042010. Advances in the long-pulse steady-state high beta H-mode scenario with active controls of divertor heat and particle fluxes in EAST; https://doi.org/10.1088/1741-4326/ac2993

[35] A. Nagy, A. Bortolon, D. M. Mauzey, E. Wolfe, E. P. Gilson, R. Lunsford, R. Maingi, D. K. Mansfield, R. Nazikian, and A. L. Roquemore, Rev Sci Instrum 89, 10K121 (**2018**). A multi-species powder dropper for magnetic fusion applications; https://doi.org/10.1063/1.5039345

[36] Z. Wang, Z. Sun, K. Wu, Y. Huang, W. Xu, Y. H. Guan, M. Huang, H. M. Zhang, J. J. Yang, Y. M. Duan *et al.*, Nuclear Fusion 65 (**2025**) 104001. Fuel recycling and impurity characteristics in long-pulse H-mode plasmas with full metal and dynamically coated walls on EAST; https://doi.org/10.1088/1741-4326/adfd71

[37] Y. Q. Tao, G. S. Xu, K. Wu, Q. Q. Yang, L. Wang, Q. P. Yuan, Y. F. Wang, X. Lin, L. Y. Meng, G. F. Ding *et al.*, Nuclear Fusion 63, 076008 (**2023**) 076008. Long-pulse H-mode operation with stored-energy monitoring for detachment feedback control with a new lower tungsten divertor in EAST; https://doi.org/10.1088/1741-4326/acd014

[38] Y. M. Duan, L. Q. Hu, K. Y. Chen, W. Du, L. Zhang, and E. Team, Journal of Nuclear Materials 438, S338 (**2013**). Radiation distribution and energy loss during ELM in EAST; https://doi.org/10.1016/j.jnucmat.2013.01.063

[39] L. Zhang, S. Morita, Z. Xu, Z. Wu, P. Zhang, C. Wu, W. Gao, T. Ohishi, M. Goto, J. Shen *et al.*, Rev Sci Instrum 86, 123509 (**2015**). A fast-time-response extreme ultraviolet spectrometer for measurement of impurity line emissions in the Experimental Advanced Superconducting Tokamak; https://doi.org/10.1063/1.4937723

[40] J. C. Xu, L. Wang, G. S. Xu, W. Feng, H. Liu, J. B. Liu, W. Zhang, T. F. Ming, C. S. Yip, G. Z. Deng *et al.*, Ieee T Plasma Sci 46, 1331 (**2018**) 1331. Upgrade Design of Lower Divertor Langmuir Probe Diagnostic System in the EAST Tokamak; https://doi.org/10.1109/tps.2018.2794533

[41] Y. Chen, Z. Wu, W. Gao, L. Zhang, and W. Zha, Fusion Engineering and Design 88, 2825 (**2013**) 2825. Zeff first measurements in EAST with a multi-channel visible bremsstrahlung new system; https://doi.org/10.1016/j.fusengdes.2013.05.003

[42] http://open.adas.ac.uk.

[43] G. F. Ding, R. Chen, Y. Ye, G. S. Xu, X. Q. Wu, Q. Q. Yang, L. Yu, L. Y. Meng, L. Wang, X. Lin *et al.*, Nuclear Fusion 63 (**2023**) 066006. Various edge low-frequency fluctuations during

transition to a detached divertor in Experimental Advanced Superconducting Tokamak; https://doi.org/10.1088/1741-4326/acc4dd

[44] C. Bruhn, R. M. McDermott, C. Angioni, J. Ameres, V. Bobkov, M. Cavedon, R. Dux, A. Kappatou, A. Lebschy, P. Manas *et al.*, Plasma Physics and Controlled Fusion 62 (**2020**) 049501. Corrigendum: A novel method of studying the core boron transport at ASDEX Upgrade (2018 Plasma Phys. and Control. Fusion 60 085011); https://doi.org/10.1088/1361-6587/ab72e4

[45] L. Peng, Z. Sun, J. Sun, R. Maingi, G. Jia, X. Bonnin, F. Gao, G. Zuo, W. Xu, W. Wang *et al.*, J Fusion Energ 44 (**2025**). Role of E × B Drift in Divertor Detachment Control via Boron Powder Injection on EAST; https://doi.org/10.1007/s10894-025-00477-4

[46] L. Peng, Z. Sun, J.-Z. Sun, R. Maingi, F. Gao, X. Bonnin, H.-Y. Chang, W.-K. Wang, and J.-Y. Liu, Chinese Physics B 33 (**2024**) 115201. Comparative study of boron and neon injections on divertor heat fluxes using SOLPS-ITER simulations; https://doi.org/10.1088/1674-1056/ad711e

[47] L. Y. Meng, L. Wang, H. Q. Wang, G. Z. Deng, H. Si, K. D. Li, G. S. Xu, Q. P. Yuan, H. Y. Guo, D. Eldon *et al.*, Nuclear Fusion 62 (**2022**) 086027. Divertor plasma behaviors with neon seeding at different locations on EAST with ITER-like divertor; https://doi.org/10.1088/1741-4326/ac74cf

[48] X. Yang, X. Gong, J. Qian, Y. Jin, P. Manas, P. Li, C. Bourdelle, Y. Chu, B. Zhang, Y. Chen *et al.*, Nuclear Fusion 64 (**2023**) 016030. Mechanism of enhanced ion temperature by impurity seeding in EAST H-mode plasma; https://doi.org/10.1088/1741-4326/ad0795

[49] M. Marin, J. Citrin, C. Giroud, C. Bourdelle, Y. Camenen, L. Garzotti, A. Ho, M. Sertoli, and J. E. T. Contributors, Nuclear Fusion 63 (**2022**) 016019. Integrated modelling of neon impact on JET H-mode core plasmas; https://doi.org/10.1088/1741-4326/aca469

[50] A. W. Leonard, Plasma Physics and Controlled Fusion 60 (**2018**). Plasma detachment in divertor tokamaks; https://doi.org/10.1088/1361-6587/aaa7a9

[51] A. Kallenbach, M. Bernert, M. Beurskens, L. Casali, M. Dunne, T. Eich, L. Giannone, A. Herrmann, M. Maraschek, S. Potzel *et al.*, Nuclear Fusion 55 (**2015**) 053026. Partial detachment of high power discharges in ASDEX Upgrade; https://doi.org/10.1088/0029-5515/55/5/053026

[52] J. S. Park, M. Groth, R. Pitts, J.-G. Bak, S. G. Thatipamula, J.-W. Juhn, S.-H. Hong, and W. Choe, Nuclear Fusion 58 (**2018**) 126033. Atomic processes leading to asymmetric divertor detachment in KSTAR L-mode plasmas; https://doi.org/10.1088/1741-4326/aae865

[53] H. Mao, F. Ding, G. N. Luo, Z. Hu, X. Chen, F. Xu, Z. Yang, J. Chen, L. Wang, R. Ding *et al.*, Rev Sci Instrum 88, 043502 (**2017**). A multichannel visible spectroscopy system for the ITER-like W divertor on EAST; https://doi.org/10.1063/1.4979406

[54] Y. Chao, L. Xu, L. Hu, Y. Duan, T. Wang, Y. Yuan, and Y. Zhang, Chinese Physics B 29 (**2020**) 095201. Gaussian process tomography based on Bayesian data analysis for soft x-ray and AXUV diagnostics on EAST*; https://doi.org/10.1088/1674-1056/aba2e4

[55] Y. Ye, G. S. Xu, Y. Q. Tao, R. Chen, L. Wang, H. Y. Guo, H. Q. Wang, K. D. Li, L. Y. Meng, Q. Q. Yang *et al.*, Nuclear Fusion 61 (**2021**) 116032. Sustained edge-localized-modes

suppression and radiative divertor with an impurity-driven instability in tokamak plasmas; https://doi.org/10.1088/1741-4326/ac26eb

[56] S. S. Henderson, M. Bernert, D. Brida, M. Cavedon, P. David, R. Dux, O. Février, A. Järvinen, A. Kallenbach, M. Komm *et al.*, Nuclear Fusion 63 (**2023**) 086024. Divertor detachment and reattachment with mixed impurity seeding on ASDEX Upgrade; https://doi.org/10.1088/1741-4326/ace2d6

[57] F. Hitzler, M. Wischmeier, F. Reimold, and D. P. Coster, Plasma Physics and Controlled Fusion 62 (**2020**) 085013. Impurity transport and divertor retention in Ar and N seeded SOLPS 5.0 simulations for ASDEX Upgrade; https://doi.org/10.1088/1361-6587/ab9b00

[58] Z. Sun, Y. Z. Qian, R. Maingi, Y. F. Wang, Y. M. Wang, A. Nagy, K. Tritz, R. Lunsford, E. Gilson, G. Z. Zuo *et al.*, Nuclear Fusion 61, 066022 (**2021**) 066022. Type-I ELM mitigation by continuous lithium granule gravitational injection into the upper tungsten divertor in EAST; https://doi.org/10.1088/1741-4326/abf855

[59] T. H. Osborne, G. L. Jackson, Z. Yan, R. Maingi, D. K. Mansfield, B. A. Grierson, C. P. Chrobak, A. G. McLean, S. L. Allen, D. J. Battaglia *et al.*, Nuclear Fusion 55, 063018 (**2015**) 063018. Enhanced H-mode pedestals with lithium injection in DIII-D; https://doi.org/10.1088/0029-5515/55/6/063018